RESEARCH ARTICLE

MXene-Regulated Perovskite Vertical Growth for High-Performance Solar Cells

Chao Wu,[a†] Wenzhong Fang,[a,b†] Qunfeng Cheng,[b†] Jing Wan,[c] Rui Wen,[c] Yang Wang,[d] Yanlin Song,[d] Mingzhu Li[d*]

[†] These authors contributed equally to this work.

[a] Prof. C. Wu, Dr. W. Fang
School of Transportation Science and Engineering
Beihang University
Beijing 100191, P. R. China.
[b] Dr. W. Fang, Prof. Q. Cheng
Key Laboratory of Bio-inspired Smart Interfacial Science and Technology of Ministry of Education, School of Chemistry, Beijing Advanced Innovation Center for Biomedical Engineering
Beihang University
Beijing 100191, P. R. China.
[c] Dr. J. Wang, Prof. R. Wen
Key Laboratory of Molecular Nanostructure and Nanotechnology, Beijing National Laboratory for Molecular Sciences, CAS Research/Education Center for Excellence in Molecular Sciences
Institute of Chemistry, Chinese Academy of Sciences
100190 Beijing, P. R. China.
[d] Prof. Y. Wang, Prof. Y. Song and Prof. M. Li*
Key Laboratory of Green Printing
Institute of Chemistry, Chinese Academy of Sciences
Beijing 100190 P. R. China.
Email: mingzhu@iccas.ac.cn

Abstract: Defects at the interfaces of perovskite (PVK) thin films are the main factors responsible for instability and low photoelectric conversion efficiency (PCE) of PVK solar cells (PSCs). Here, a SnO_2-MXene composite electron transport layer (ETL) is used in PSCs to improve interfacial contact and passivate defects at the SnO_2/perovskite interface. The introduced MXene regulates SnO_2 dispersion and induces a vertical growth of PVK. The lattice matching of MXene and perovskite suppresses the concentration of interfacial stress, thereby obtaining a perovskite film with low defects. Compared with SnO_2-based device, the PCE of SnO_2-MXene-based device is improved by 15% and its short-circuit current is up to 25.07 mA cm^{-2}. Furthermore, unencapsulated device maintained about 90% of its initial efficiency even after 500 h of storage at 30–40% relative humidity in the air. The composite ETL strategy provides a route to engineer interfacial passivation between metal halide perovskites and ETLs.

Introduction

In recent years, PSCs have achieved a PCE of up to 25.7%,[1] and they are regarded as one of the most promising large-scale photovoltaic materials for a future energy source. The high efficiency of PSCs is achieved through efficient charge extraction without nonradiative recombination at the charge transport and perovskite interfaces.[2] It has been shown that passivation of the top contact perovskite surface with long-chain organic salts substantially reduces interfacial defects between the hole-transporting layer and perovskite.[3, 4] However, due to the solvent incompatibility and high-temperature processing, investigation on the bottom interface passivation of perovskite is lagging.[5] The ETL plays a crucial role in extracting and transporting photogenerated electron carriers and serves as a hole-blocking layer by suppressing charge recombination. Therefore, many experimental efforts focus on finding novel robust inorganic ETLs such as TiO_2, SnO_2, and ZnO.[5] Recently, SnO_2 ETLs, which take advantage of low-temperature annealing (150 °C) and good energy-level alignment with perovskite and the electrodes, have been spotlighted.[6-8] However, SnO_2 nanoparticles are colloidally unstable due to van der Waals interaction between particles. Unstable nanoparticles tend to form large agglomerates and reduce the quality of film formation.[9] Besides easy agglomeration, the electron mobility of SnO_2 (10^{-3} cm^2 V^{-1} S^{-1}) does not match the perovskite (0.5–30 cm^2 V^{-1} S^{-1}),[10] and the low-temperature synthesis environment also causes a large number of trap defects.[11] Therefore, efforts toward SnO_2 layer modification are urgently needed to address these bottlenecks. The interface modification of organic molecules (e.g., heparin potassium, EDTA, carbon dots)[12-15] or inorganic compounds (e.g., GO, metal ions)[16-18] is considered to be an effective strategy to solve the surface trap state and interface matching of SnO_2 and the bottom perovskite.

MXene is a new two-dimensional carbon-containing inorganic compound with the general formula $M_{n+1}X_nT_x$ (n = 1,2,3), where M stands for a transition metal, X stands for a carbon or nitrogen atom, and T_x is a surface functional group.[19] In recent years, MXene has been widely used in PSCs due to its unique photoelectric properties and adjustable surface functional groups.[20-26] Carlo et al. improved interfacial energy-level matching and reduced carrier recombination by tuning MXene surface functional groups and mixing MXene with the ETL and perovskite.[20] Huang et al. introduced MXene into SnO_2 to form an effective heterojunction structure (called a multi-dimensional conductive network structure), which led to an increase in the conductivity of the SnO_2 film.[23] Yang et al. used MXene treated with ultraviolet ozone as the ETL layer, which enhanced the extraction and transmission of electrons at the ETL/perovskite interface.[24] Xu et al. introduced Nb_2C MXenes as an external additive for SnO_2 ETL, which improved roughness, surface

energy, and defects of the SnO_2 film.[25] Obviously, MXene is an excellent interface doping material for optoelectronic devices, but the physical and chemical mechanism of MXene as an interfacial passivator between SnO_2 and perovskite has not been thoroughly explored.

Here, we introduced MXene to tune the dispersion of SnO_2 nanocrystals and found that MXene-doped SnO_2 lets perovskite crystals grow vertically on its surface and maximizes the interface matching of SnO_2 and perovskite, which gives rise to a significant improvement of PSC device performance. This method increased the conductivity of the SnO_2 ETL from 9.62×10^{-5} S cm^{-1} to 1.85×10^{-4} S cm^{-1}. Through a series of optical and electrical characterizations, we theoretically and experimentally demonstrated that the MXene contribution for inhibiting the stress concentration during the growth of perovskite is a result of its lattice matching with that of perovskite as well as improving the conductivity of the SnO_2 ETL. Compared with the SnO_2-based device, the SnO_2-MXene-based PSC achieves a 15% PCE boost and maintain about 90% of its initial efficiency even after 500 hours of storage at 30–40% relative humidity in the air.

Results and Discussion

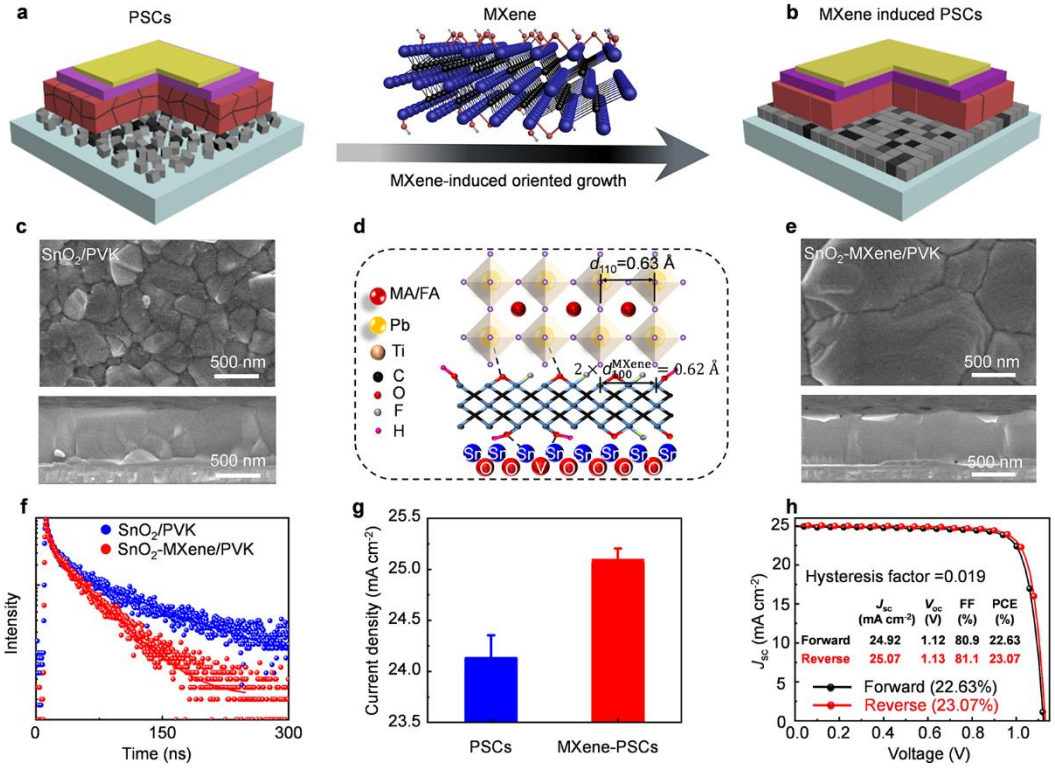


Figure 1. Structural characterization of MXene-PSCs. a), b) Structural models of PSCs and MXene-PSCs films. MXene induces vertical growth of perovskite and enhances interfacial contact between perovskite and SnO_2. c), e) SEM images of cross-sections and top for SnO_2/PVK and SnO_2-MXene/PVK. The average grain of SnO_2-MXene/PVK (~1 μm) is three times the size of SnO_2/PVK grain (~356 nm). d) Detailed diagram of the mechanism of MXene bridging SnO_2 and PVK. Lattice matching of MXene (3.1 Å) and CsFAMA perovskite (6.3 Å) enables high-quality vertical growth of perovskite. f) Time-resolved PL decays of SnO_2/PVK and SnO_2-MXene/PVK films. g) Current density of PSCs and MXene-PSCs. The J_{sc} of the MXene-PSCs (J_{sc} = 25.07 mA cm^{-2}) is higher than the original PSCs (J_{sc} = 24.16 mA cm^{-2}). h) J-V hysteresis of the MXene-PSC. The MXene-PSC show a negligible photocurrent hysteresis.

Figure 1a and b illuminate the vertical crystallization of perovskites using MXene-doped SnO_2 ETL. The SnO_2-MXene based perovskite (SnO_2-MXene/PVK) presents itself as a large-size and vertically grown crystal (Figure 1e). An average grain of SnO_2-MXene/PVK (~1 μm in size) is three times the size of a SnO_2/PVK grain (~356 nm) (Figure 1c, Supplementary Figure 1). Figure 1d is an illustration of the mechanism of MXene bridging SnO_2 and perovskite in planar solar cells. MXene can maximize the matching between SnO_2 and perovskite regarding electron extraction rate and interface contact towards enhancing the crystalline quality of perovskites and subsequent photovoltaic performance. The van der Waals interaction between neighboring SnO_2 nanocrystals is weakened due to the Lewis acid-base interaction between -OH on the surface of MXene and Sn atoms in SnO_2, inhibiting the agglomeration of SnO_2 nanocrystals. The lattice spacing (6.3 Å) of CsFAMA (FA: $CH(NH_2)^{2+}$; MA: CH_3NH^{3+}) perovskite (100)[27] is very close to two times the lattice spacing of MXene (3.1 Å). The lattice matching of MXene and perovskite can suppress stress concentration during perovskite growth to result in high-quality PVK films with lower defect density.[28] In addition, the -O on the surface of MXene passivates the excess Pb in the perovskite, reducing the possibility of carrier recombination at the interface between the SnO_2 and the perovskite bottom. According to the time-resolved PL results (Figure 4f), the lifetime of SnO_2-MXene/PVK (τ_1 is 17.34 ns, τ_2 is 48.20 ns) is much shorter than the lifetime of SnO_2/PVK (τ_1 is 20.73 ns, τ_2 is 80.24 ns), indicating a better charge extraction of the SnO_2-MXene ETL than the pristine SnO_2 ETL. Compared with the conductivity of the SnO_2 film (σ_{SnO2} = 9.62×10^{-5} S cm^{-1}), the conductivity of the SnO_2-MXene film is increased to 192% ($\sigma_{SnO2\text{-}MXene}$ = 1.85×10^{-4} S cm^{-1})

due to the excellent conductivity of MXene (Supplementary Figure 2, Supplementary Table 1). Consequently, the current of the MXene-PSCs (J_{sc} = 25.07 mA cm^{-2}) is higher than the original PSCs (J_{sc} = 24.16 mA cm^{-2}). Simultaneously, the MXene-PSC almost have a negligible hysteresis with a low hysteresis factor (0.019), as shown in Figure 1h.

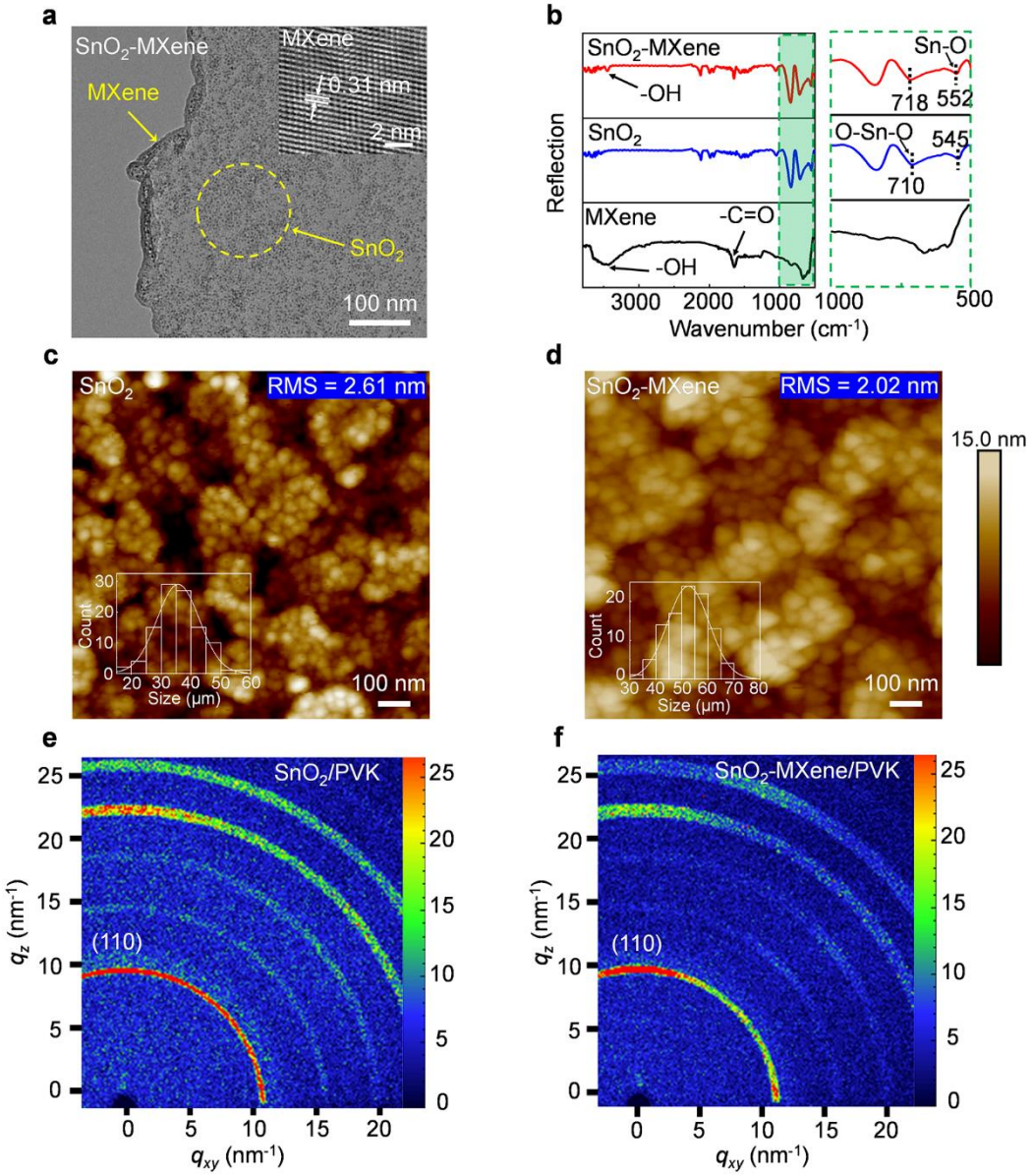


Figure 2. Crystallization dynamics of perovskites under the SnO_2 and SnO_2-MXene films. a) Transmission Electron Microscope (TEM) image of SnO_2-MXene solution (MXene's lattice spacing d_{100}=0.31 nm). SnO_2 nanocrystals are uniformly dispersed on MXene. b) The infrared spectrum of MXene, SnO_2 and SnO_2-MXene film. Lewis adducts are formed between SnO_2 and MXene. c), d) Atomic force microscopy (AFM) images of the SnO_2 and SnO_2-MXene films, respectively. SnO_2-MXene (~52 nm) films show larger particle sizes than pristine SnO_2 (~35 nm) films. e), f) GIWAXS patterns of SnO_2/PVK and SnO_2-MXene/PVK film. SnO_2-MXene induces oriented growth of PVK.

As shown in Figure 2a, SnO_2 nanoparticles are uniformly dispersed on MXene. The zeta potential of the SnO_2-MXene ([MXene] = 0.25 mg ml^{-1}) solution (zeta potential −42.4 ± 1.84 mV) is about twice that of the pristine SnO_2 solution (zeta potential −21.9 ± 0.95 mV), indicating better dispersion and stability (Supplementary Figure 4 and Supplementary Table 2).[29] High-resolution transmission electron microscope (HR-TEM) images and selected area electron diffraction patterns of MXene nanosheets show the expected basal hexagonal structure, 0.31 nm interplanar spacing, and no nano-scale defects (inset Figure 2a and Supplementary Figure 5). Supplementary Figure 6 shows the preparation process of MXene based on HCl and LiF etching to achieve nanoflakes. Supplementary Figure 7 shows the XRD of MXene after etching. The XPS spectrum shows that the surface of MXene has -OH, -O, -F functional groups after successful etching (Supplementary Figure 8). Supplementary Figure 9 shows the energy-dispersive X-ray spectroscopy (EDX) elemental mapping of SnO_2-MXene films, revealing that the Ti, F, Sn, and C elements were uniformly distributed in the selected area. FTIR was used to study the interaction between SnO_2 and MXene. As shown in Figure 2b, the peaks around 3440 cm^{-1} belong to -OH stretching vibration in the MXene. The characteristic peaks of SnO_2 observed at 705 cm^{-1} and 544 cm^{-1} are due to the O-Sn-O stretch and the Sn-O vibration, respectively.[12] For the SnO_2-MXene sample, the characteristic peaks of SnO_2 shift to 713 cm^{-1} and 553 cm^{-1}, and the -OH

stretching vibration peaks shift to 3445 cm^{-1}, demonstrating that the MXene is indeed complexed with SnO_2. Simultaneously, the Sn 3d3/2 (~486.50 eV) and Sn 3d5/2 (~495.05 eV) peaks of pristine SnO_2 shifted to lower positions at ~485.99 eV and ~494.41 eV after incorporating with MXene (Supplementary Figure 10). This finding further confirms that Lewis adducts are formed between SnO_2 and MXene. The formation of adducts can reduce the van der Waals interaction between neighboring SnO_2 nanocrystals, inhibiting SnO_2 nanocrystal agglomeration.[12, 13]

Besides stabilizing the SnO_2 dispersions, MXene also serves as a template to enhance the crystallization of SnO_2 nanocrystals on ITO substrates. As shown in the AFM images (Figure 2c and d, Supplementary Figure 11), the SnO_2-MXene film showed a larger particle size (~52 nm) than the pristine SnO_2 film (~35 nm). It is worth noting that when the crystallinity of SnO_2 nanocrystals increases, the roughness slightly decreases (Figure 2c) due to the uniformly dispersed SnO_2 nanocrystals. The XRD peak intensity of SnO_2-MXene is significantly enhanced, which further confirms that MXene enhances the crystallinity of SnO_2 nanocrystals (Supplementary Figure 12). The transmission of the SnO_2-MXene film is around 86% on average over the broad wavelength range from 400 nm to 500 nm, close to that of the SnO_2 films (~87% on average), so that the increase in the size of SnO_2 particles does not affect the transparency of the SnO_2 film (Supplementary Figure 13).

The quality of the perovskite films, including grain size, crystallinity, surface coverage, etc., is very important for high-performance PSCs. A smaller contact angle results in reduced Gibbs free energy for heterogeneous nucleation, which is conducive to the formation of dense and flat perovskite films.[30] As shown in Supplementary Figure 14, the SnO_2-MXene ([MXene] = 0.25 mg ml^{-1}) film (CA ~18.5°) shows a smaller contact angle than the SnO_2 film (CA ~35.3°), so the perovskite solution on the SnO_2-MXene substrate is more prone to nucleation, leading to the formation of denser and highly crystalline perovskite. Suitable nucleation density will promote the film densification process. However, when MXene is excessive, the perovskite grain size decreases sharply (Supplementary Figs. 15 and 16). This is because the excessive MXene increases nucleation sites of PVK, resulting in competition among perovskite seeds, uneven growth, and increased crystallization stress.[13] Perovskite formation is the combination of nucleation and crystal growth processes. Generally, rapid nucleation followed by a slow crystal growth is essential for forming high-quality perovskite films with more surface coverage and fewer defects. Forming a Lewis acid-base adduct is a simple but effective strategy to retard the crystallization of a perovskite.[31] The -O groups in MXene form an intermediate adduct with PbI_2 of perovskite, as revealed by the XPS in Supplementary Figure 17. The Pb 4f peaks of the SnO_2-MXene/PVK were shifted towards lower binding energy (134.3 eV, 138.4 eV) compared with the control film (134.4 eV, 138.6 eV). This is because Pb atoms coordinate with MXene to form Ti-O-Pb bonds, and the surrounding electron cloud density increases.[32] MXene significantly delayed PVK growth due to the formation of adducts,[33] which encouraged PVK to grow to a more thermodynamically favorable state, and therefore formed a higher ordering and larger crystallinity of PVK grains. Simultaneously, the slow growth of PVK also provides time for Oswald ripening. Small-grained perovskites are more easily dissolved during the growth process due to their relatively high chemical potential. Therefore, large grain coarsening occurs upon the adsorption of small grains (dissolution of small grains), which is terminated until the evaporation of the solvent in the intermediate is complete. Rapid nucleation followed by a slow crystal growth forms high-quality perovskite films with more surface coverage and fewer defects.

The interface strain relaxation theory reveals the reason for the directional high-quality growth of the perovskite layer. Usually, perovskite lattice distortion induced by interface lattice mismatch between the SnO_2 and perovskite film causes a sluggish charge extraction and transfer dynamics in CsFAMA PSCs.[34] In our work, the two times lattice spacing of MXene (3.1 Å) is very close to the CsFAMA perovskite lattice spacing (6.3 Å)[28] (Figure 2a). The lattice matching of MXene and CsFAMA perovskite can suppress stress concentration during perovskite growth. The GIWAXS pattern of SnO_2-MXene/PVK has a brighter scattering ring at $q \approx 10.0$ nm^{-1}, as shown in Figure 2e and f. The azimuthal integrated 1D GIXRD spectrum (Supplementary Figure 18a) and the radial integrated intensity map along the (110) diffraction ring (Supplementary Figure 18b) show that the SnO_2-MXene/PVK film has a higher and sharper (110) diffraction peak than the SnO_2/PVK film. These results indicate that SnO_2-MXene/PVK has better crystallinity and out-of-plane orientation.[35, 36] Therefore, the lattice matching of MXene and perovskite suppresses the stress concentration caused by the interface mismatch in the annealing and cooling process of the perovskite, resulting in high-quality oriented perovskite films.

Meanwhile, we have studied the effects of different size distributions and concentrations of MXene on devices performance. The PCE of devices reach the optimal value of 22.63% with MXene-SnO_2 ETL made from 0.10 mg ml^{-1} MXene (7.9 ± 0.31 μm) mixed SnO_2 solution (Figure 3a and Supplementary Figure 22). It is demonstrated that larger MXene results in better performance, including fewer defects and better conductivity.[37] The device obtains the optimal PCE of 23.07% (Figure 3b and Supplementary Figure 23) when the MXene size is 7.9 ± 0.31 μm ([MXene] = 0.25 mg ml^{-1}). Therefore, the optimal concentration of MXene (0.25 mg ml^{-1}) and size (7.9 ± 0.31 μm) were used to fabricate the best performing device.

Due to the lattice matching of MXene and CsFAMA PVK, the SnO_2-MXene substrate can significantly reduce the stress concentration during perovskite growth.[38-40] As shown in Figure 3c, the main peak (110) (14.19°) of SnO_2-MXene/PVK slightly shifted to lower angles (14.15°). As the concentration of MXene increased, the position of the main peak of PVK gradually shifted to lower angles (Supplementary Figure 24). The (110) peak of the SnO_2-MXene/perovskite shift is attributed to the SnO_2-MXene substrate eliminating the stress during the growth of the perovskite crystal. Ultraviolet-visible absorption spectra show that the absorption intensity of SnO_2-MXene/PVK films in the range of 300–650 nm is higher than that of SnO_2/PVK films (Supplementary Figure 25), which can be attributed to the extra absorption of MXene and higher quality PVK films.[41] The electron extraction capability of SnO_2-MXene film was further studied by PL. The SnO_2-MXene/PVK has lower PL emissions than SnO_2/PVK (Figure 3d), which indicates enhanced extraction of carriers and reduced carrier recombination, consistent with the TRPL results.

We assess the defect-states of the SnO_2-MXene/PVK films through the space-charge-limited current (SCLC) method. The SCLC device exhibits a linear ohmic response under a low bias

voltage. When the applied voltage exceeds the kink point, the current is significantly enhanced because the trap state of the film is filled with carriers. Therefore, the kink voltage is also called the trap-filled limit voltage (V_{TFL}), and the trap density (N_t) can be calculated by equation (1):

$$V_{TFL} = eN_tL^2 / 2\varepsilon\varepsilon_0 \quad (1)$$

Where e, ε, ε_0, and L represent the basic charge, relative permittivity of perovskite, vacuum permittivity, and thickness of the perovskite film (Supplementary Figure 26), respectively. The dielectric constant ε is 62.23. Compared to SnO_2/PVK (N_t = 6.91×10^{15} cm^{-3}), SnO_2-MXene/PVK (N_t = 4.79×10^{15} cm^{-3}) has a lower trap density (Figure 3e). The low trap density is responsible for improving the photoelectric performance of the device.

Table 1 Photovoltaic performance parameters of champion pristine PSC and MXene-PSC.

ETLs	Scan direction	V_{oc} (V)	J_{sc} (mA cm^{-2})	FF	PCE
SnO_2	Reverse	1.09	24.16	75.8%	20.03%
	Forward	1.07	23.83	71.7%	18.40%
SnO_2-MXene	Reverse	1.13	25.07	81.1%	23.07%
	Forward	1.12	24.92	80.9%	22.63%

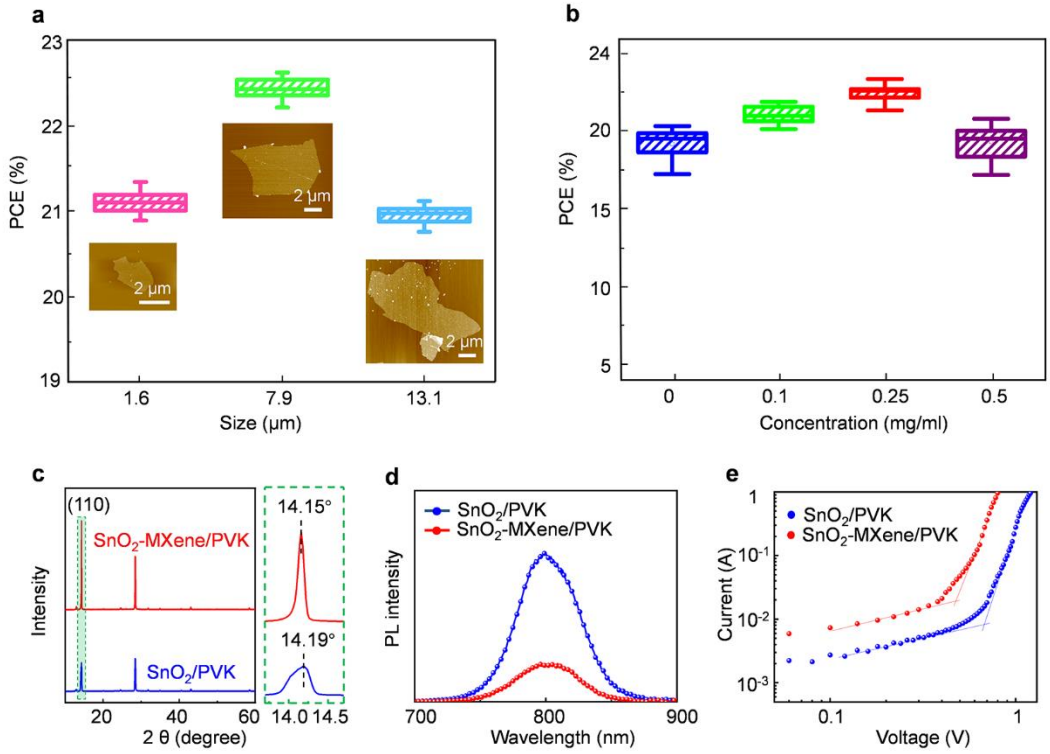


Figure 3. Characterization of perovskite films and PCE of PSCs. a) PCE of devices with different MXene sizes: 1.6 ± 0.11 μm, 7.9 ± 0.31 μm, 13.1 ± 0.28 μm. At a concentration of 0.10 mg ml^{-1}, the device achieves an efficiency of 22.63% at an MXene size of 7.9 ± 0.31 μm. b) PCE of devices with different MXene (7.9 ± 0.31 μm) concentration: 0 mg ml^{-1}, 0.1 mg ml^{-1}, 0.25 mg ml^{-1}, 0.5 mg ml^{-1}. The size of MXene is 7.9 ± 0.31 μm, and the device achieves 23.07% efficiency at a concentration of 0.25 mg ml^{-1}. c) XRD patterns of the perovskite film based on SnO_2 with and without MXene modification. d) PL spectra of PVK deposited on pristine SnO_2 and SnO_2-MXene, respectively. e) Dark J-V curves of electron-only devices based on SnO_2 and SnO_2 ETLs.

Kelvin probe force microscopy (KPFM) has been proven to be a useful method for probe interface energetics in PSCs.[42] Therefore, we employed KPFM to examine the potential distribution along the device cross-section under short-circuit conditions (Supplementary Figure 27). Figure 4 a and b are KPFM results of pristine PSC and MXene-PSC, respectively, together with corresponding cross-sectional AFM images and contact potential difference (CPD) profiles. The relevant AFM image is shown in Supplementary Figure 28. The section is relatively clear, excluding the influence of the surface morphology on the CPD results.[43] The slope represents the driving force for carrier separation.[44] Compared with the small CPD drop at the SnO_2/PVK interface, the drop magnitude at the SnO_2-MXene/PVK interface is much larger (137 mV vs. 39 mV). Based on the above results, we can deduce that the SnO_2-MXene/PVK interface is beneficial to the separation and extraction of excitons. In order to consider the carrier extraction capability of the device in the working state,[45] we then further studied the effects of the SnO_2-Mxene ETL on the charge carrier transport and recombination characteristics in complete devices by measuring charge carrier extraction time and the charge carrier lifetime via transient photocurrent (TPC) and transient photovoltage (TPV) methods, respectively. In Supplementary Figure 29a, the photocurrent decay time of SnO_2-MXene PSC under short-circuit condition is reduced to 0.76 μs, compared with 1.37 μs of SnO_2 PSC. The high charge carrier extraction capability of SnO_2-MXene ETL reduced charge carrier extraction time by 1.8 times, thus benefiting the efficient charge carrier separation and extraction. Additionally, the SnO_2-MXene PSC exhibited the longest electron lifetime of 4.65 μs (Supplementary Figure 29 b), indicating that SnO_2-MXene ETL suppresses interfacial nonradiative recombination.

The proper energy band arrangement of an ETL is conducive to the charge extraction in the ETL/perovskite interface and the increase of the open-circuit voltage (V_{oc}) of the device.[46] Figure 4c provides a schematic energy-level diagram of each layer. The

values of the work function (WF) of pristine SnO_2 and SnO_2-MXene are approximately 3.77 eV (= *hv*−17.44 eV, where *hv* = 21.21 eV is the incident photon energy) and 4.01 eV (*hv*−17.20 eV), respectively (Supplementary Figure 30 and 31). After the introduction of MXene, the maximum value of the valence band (Ev) shifted downward (Figure 4c), from −7.72 eV (SnO_2) to −7.93 eV (SnO_2-MXene). Compared with the SnO_2-ETL, the downshift of the valence band of the SnO_2-MXene-ETL improves the ability to suppress hole recombination and hinders the hole migration to the ITO electrode. Overall, the findings prove that through the introduction of MXene, perovskite films with enhanced photoelectric properties are obtained, which plays a leading role in obtaining efficient and stable perovskite solar devices.

In the visible light range, the MXene-PSC has higher EQE than pristine PSC, indicating improved light utilization (Figure 4d). It is worth noting that the integrated current values of the pristine PSC and the MXene-PSC are 23.61 mA cm^{-2} and 24.77 mA cm^{-2}, respectively, which are consistent with the *J-V* results. To further prove the quality of the device, the dependence of V_{oc} on light intensity was studied (Supplementary Figure 32). The deviation of the slope from *KT*/*q* (where *k* is the Boltzman constant, *T* is the absolute temperature, and *q* is the basic charge) reveals the trap-assisted recombination in photovoltaic devices. As the light intensity decreases, V_{oc} decreases proportionally. The slope (1.57 *kT*/*q*) exhibited by the MXene-PSC is smaller than that of the pristine PSC (2.19 *kT*/*q*), which indicates that the nonradiative recombination of the device is reduced.

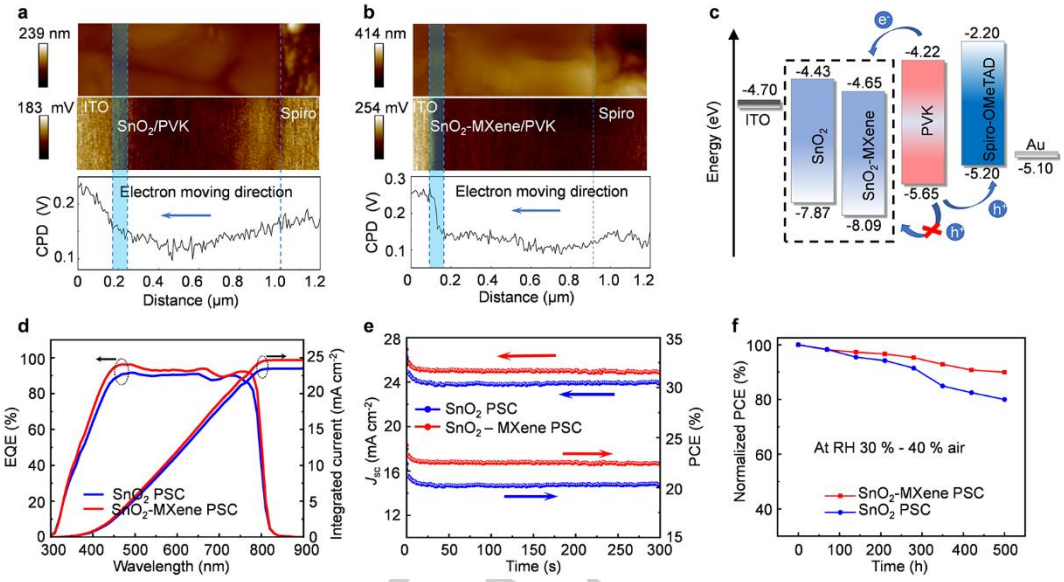


Figure 4. Characterization of the PSCs. AFM image, KPFM image and CPD profile of the a) SnO_2/PVK and b) SnO_2-MXene/PVK interfaces, from top to bottom, respectively. The drop at the SnO_2-MXene/PVK (137 mV) interface is larger than that at the SnO_2/PVK interface (39 mV). c) Energy level diagram of the device interface. SnO_2-MXene interface can better hinder hole transport. d) EQE of the pristine PSC, SnO_2-MXene PSC, and integrated short-circuit current density. e) Steady-state current density and PCE versus time for the best-performing devices using SnO_2 and SnO_2-MXene-based, respectively, measured at the maximum power point. f) Long-term stability of the pristine and SnO_2-MXene PSC in air (RH = 30% - 40%) at room temperature without encapsulation.

In order to study the stability, we tested the continuous maximum power point tracking (MPPT) of MXene-PSC (V_{max} = 0.9 V) for 300 s under one continuous sunlight exposure (AM1.5, 100 mW cm^{-2}) (Figure 4e). Under a fixed bias, the PCE of the pristine PSC and MXene-PSC stabilized at 19.84% and 22.50%, respectively, which were very close to the measured value of the J-V curve. Figure 4f shows the environmental stability of unpackaged PSC stored in an environment with a relative humidity (RH) of 30% ~ 40% at room temperature. Due to the high-quality contact between the SnO_2-MXene and the perovskite layer, after 500 hours of storage, the PCE of the MXene-PSC remains at 90% of its initial value, while the performance of the pristine PSC drops to 80% of its initial value. For rapid aging experiments, a stability test of device was conducted under simulated white LED (power is 500 W) illumination at 30% RH for 500 h (without encapsulation). The decomposition rate of SnO_2 PSC is higher than that of SnO_2-MXene PSC, and the PbI_2 phase is evident in SnO_2 PSC, while the decomposition of SnO_2-MXene PSC is negligible (Supplementary Figure 33). Supplementary Figure 34 shows the light stability of the PSC under simulated one-sun illumination (LED) in a glove box, which proves that the SnO_2-MXene PSC is much more resistant to light stress than the SnO_2 PSC. There are less than 10% efficiency losses after 300 h continuous simulated one-sun illumination for SnO_2-MXene PSC, whereas the measured PCEs presented over 50% losses for the SnO_2 PSC under the same conditions. Supplementary Figure 35 shows the thermal stability test of the device by annealing them at ~85°C for 300 hours in N_2. Notably, the PCE of the SnO_2-MXene PSC dropped much less compared with the SnO_2 PSC, demonstrating that the novel SnO_2-MXene ETL enhances the thermal stability of planar PSC significantly over those based on a pristine SnO_2 ETL. To compare the performance of the same type of perovskite device, we have counted the PCE and J_{sc} of the CsFAMA perovskite device in the past three years, as shown in Supplementary Figure 36, and the specific parameter values are shown in Supplementary Table 7. The red five-pointed star mark represents this work. Compared with other similar research results, our device performs very well in terms of J_{sc} (25.07 mA cm^{-2}) and PCE (23.07%) parameters.

Conclusion

We have presented an effective strategy to simultaneously modify the electronic property of the SnO_2 and passivate the interface

between the perovskite and the SnO_2 by introducing MXene. We find that the lattice matching of MXene and perovskite is able to induce vertically aligned crystal growth of perovskites by suppressing the generation of concentrated stress during the growth of the perovskite. In addition, the introduction of the MXene not only reduces surface defects in the SnO_2 film, but also builds a bridge for electron transport from perovskite film to SnO_2 ETL, thus resulting in significantly suppressed electron accumulation. Correspondingly, the J_{sc} of SnO_2-MXene-based PSC is as high as 25.07 mA cm^{-2} with negligible hysteresis. Compared with SnO_2-based devices, the PCE of SnO_2-MXene-based devices is improved by 15% (23.07%) with 90% of its initial efficiency under 500 hours of storage at 30–40% relative humidity in the air. In this work, the lattice matching of MXene and perovskite provides a reference for the use of similar materials in the precise interfacial engineering of perovskite-related devices.

Supporting Information

All data are available in the main text or the supplementary materials.

Acknowledgements

We thank W. Bu and G. Song at CAS Key Laboratory of Engineering Plastics, the Institute of Chemistry, Chinese Academy of Sciences, for the GIWAX measurements, F. Vogelbacher at Key Laboratory of Green Printing, Institute of Chemistry, Chinese Academy of Sciences, for his writing assistance, and B. Guan at Analysis and Testing Center, the Institute of Chemistry, Chinese Academy of Sciences, for the HRTEM measurements.

Funding: This work was supported by the National Key Research and Development Program of China (Grant No. 2021YFA0715700), the National Science Fund for Distinguished Young Scholars (Grant No. 52125302), National Natural Science Foundation of China (Grants No. 22075009, 51961130388, 21875010, 51522301, 21273017, 51103004), Newton Advanced Fellowship (Grant No. NAF\R1\191235), Beijing Natural Science Foundation (Grant No. JQ19006), and 111 Project (Grant No. B14009).

Conflict of interest

The authors declare no conflict of interest.

Keywords: interfaces • perovskite • solar cells • MXene • SnO_2

[1] National Renewable Energy Laboratory, “Best research-cell efficiency chart”, www.nrel.gov/pv/cell-efficiency.html, **2022**.

[2] H. Min, D. Y. Lee, J. Kim, G. Kim, K. S. Lee, J. Kim, M. J. Paik, Y. K. Kim, K. S. Kim, M. G. Kim, T. J. Shin, S. Il Seok, *Nature* **2021**, 598, 444.

[3] T.-H. Han, J.-W. Lee, C. Choi, S. Tan, C. Lee, Y. Zhao, Z. Dai, N. De Marco, S.-J. Lee, S.-H. Bae, Y. Yuan, H. M. Lee, Y. Huang, Y. Yang, *Nat. Commun.* **2019**, 10, 520.

[4] Q. Jiang, Y. Zhao, X. Zhang, X. Yang, Y. Chen, Z. Chu, Q. Ye, X. Li, Z. Yin, J. You, *Nat. Photonics* **2019**, 13, 460.

[5] T. Bu, J. Li, F. Zheng, W. Chen, X. Wen, Z. Ku, Y. Peng, J. Zhong, Y.-B. Cheng, F. Huang, *Nat. Commun.* **2018**, 9, 4609.

[6] A. Agresti, S. Pescetelli, A. L. Palma, A. E. Del Rio Castillo, D. Konios, G. Kakavelakis, S. Razza, L. Cinà, E. Kymakis, F. Bonaccorso, A. D. Carlo, *ACS Energy Lett.* **2017**, 2, 279.

[7] C. Petridis, G. Kakavelakis, E. Kymakis, *Energy Environ. Sci.* **2018**, 11, 1030.

[8] Y. Rong, Y. Hu, A. Mei, H. Tan, M. I. Saidaminov, S. Il Seok, M. D. McGehee, E. H. Sargent, H. Han, *Science* **2018**, 361, 1214.

[9] J. Wei, F. Guo, X. Wang, K. Xu, M. Lei, Y. Liang, Y. Zhao, D. Xu, *Adv. Mater.* **2018**, 30, 1805153.

[10] R. L. Milot, G. E. Eperon, H. J. Snaith, M. B. Johnston, L. M. Herz, *Adv. Funct. Mater.* **2015**, 25, 6218.

[11] Q. Jiang, X. Zhang, J. You, *Small* **2018**, 14, 1801154.

[12] S. You, H. Zeng, Z. Ku, X. Wang, Z. Wang, Y. Rong, Y. Zhao, X. Zheng, L. Luo, L. Li, S. Zhang, M. Li, X. Gao, X. Li, *Adv. Mater.* **2020**, 32, 2003990.

[13] D. Yang, R. Yang, K. Wang, C. Wu, X. Zhu, J. Feng, X. Ren, G. Fang, S. Priya, S. F. Liu, *Nat. Commun.* **2018**, 9, 3239.

[14] B. Tu, Y. Shao, W. Chen, Y. Wu, X. Li, Y. He, J. Li, F. Liu, Z. Zhang, Y. Lin, X. Lan, L. Xu, X. Shi, A. M. C. Ng, H. Li, L. W. Chung, A. B. Djurišic, Z. He, *Adv. Mater.* **2019**, 31, 1805944.

[15] W. Hui, Y. Yang, Q. Xu, H. Gu, S. Feng, Z. Su, M. Zhang, J. Wang, X. Li, J. Fang, F. Xia, Y. Xia, Y. Chen, X. Gao, W. Huang, *Adv. Mater.* **2020**, 32, 1906374.

[16] S. Zhang, H. Si, W. Fan, M. Shi, M. Li, C. Xu, Z. Zhang, Q. Liao, A. Sattar, Z. Kang, Y. Zhang, *Angew. Chem. Int.* Edit. **2020**, 59, 11573; *Angew. Chem.* **2020**,132,11670.

[17] L. Xiong, Y. Guo, J. Wen, H. Liu, G. Yang, P. Qin, G. Fang, *Adv. Funct. Mater.* **2018**, 28, 1802757.

[18] Z. Liu, K. Deng, J. Hu, L. Li, *Angew. Chem. Int. Ed.* **2019**, 58, 11497; *Angew. Chem.* **2019**,131,11621.

[19] A. Lipatov, H. Lu, M. Alhabeb, B. Anasori, A. Gruverman, Y. Gogotsi, A. Sinitskii, *Sci. Adv.* **2018**, 4, eaat0491.

[20] A. Agresti, A. Pazniak, S. Pescetelli, A. Di Vito, D. Rossi, A. Pecchia, M. Auf der Maur, A. Liedl, R. Larciprete, D. V. Kuznetsov, D. Saranin, A. Di Carlo, *Nat. Mater.* **2019**, 18, 1228.

[21] D. Saranin, S. Pescetelli, A. Pazniak, D. Rossi, A. Liedl, A. Yakusheva, L. Luchnikov, D. Podgorny, P. Gostischev, S. Didenko, A. Tameev, D. Lizzit, M. Angelucci, R. Cimino, R. Larciprete, A. Agresti, A. Di Carlo, Nano Energy 2021, 82, 105771.

[22] T. Chen, G. Tong, E. Xu, H. Li, P. Li, Z. Zhu, J. Tang, Y. Qi, Y. Jiang, J. Mater. Chem. A 2019, 7, 20597.

[23] L. Huang, X. Zhou, R. Xue, P. Xu, S. Wang, C. Xu, W. Zeng, Y. Xiong, H. Sang, D. Liang, *Nano-Micro Lett.* **2020**, 12, 44.

[24] L. Yang, C. Dall'Agnese, Y. Dall'Agnese, G. Chen, Y. Gao, Y. Sanehira, A. K. Jena, X. F. Wang, Y. Gogotsi, T. Miyasaka, Adv. Funct. Mater. 2019, 29, 1905694.

[25] Y. Niu, C. Tian, J. Gao, F. Fan, Y. Zhang, Y. Mi, X. Ouyang, L. Li, J. Li, S. Chen, Y. Liu, H. Lu, X. Zhao, L. Yang, H. Ju, Y. Yang, C. Ding, M. Xu, Q. Xu, Nano Energy 2021, 89, 106455.

[26] Y. Yang, H. Lu, S. Feng, L. Yang, H. Dong, J. Wang, C. Tian, L. Li, H. Lu, J. Jeong, S. Zakeeruddin, Y. Liu, M. Gratzel, A. Hagfeldt, Energy Environ. Sci. 2021, 14, 3447.

[27] Q. Cao, J. Yang, T. Wang, Y. Li, X. Pu, J. Zhao, Y. Zhang, H. Zhou, X. Li, X. Li, *Energy Environ. Sci.* **2021**, 14, 5406.

[28] G. Tang, P. You, Q. Tai, A. Yang, J. Cao, F. Zheng, Z. Zhou, J. Zhao, P. K. L. Chan, F. Yan, *Adv. Mater.* **2019**, 31, 1807689.

[29] M. G. Trulli, E. Sardella, F. Palumbo, G. Palazzo, L. C. Giannossa, A. Mangone, R. Comparelli, S. Musso, P. Favia, *J. Colloid. Interface. Sci.* **2017**, 491, 255.

[30] W. Hui, Y. Yang, Q. Xu, H. Gu, S. Feng, Z. Su, M. Zhang, J. Wang, X. Li, J. Fang, *Adv. Mater.* **2020**, 32, 1906374.

[31] D.-Y. Son, J.-W. Lee, Y. J. Choi, I.-H. Jang, S. Lee, P. J. Yoo, H. Shin, N. Ahn, M. Choi, D. Kim, N.-G. Park, *Nat. Energy* **2016**, 1, 16081.

[32] J. Li, T. Jiu, S. Chen, L. Liu, Q. Yao, F. Bi, C. Zhao, Z. Wang, M. Zhao, G. Zhang, Y. Xue, F. Lu, Y. Li, *Nano Lett.* **2018**, 18, 6941.

[33] A. A. Zhumekenov, V. M. Burlakov, M. I. Saidaminov, A. Alofi, M. A. Haque, B. Turedi, B. Davaasuren, I. Dursun, N. Cho, A. M. El-Zohry, M. D. Bastiani, A. Giugni, B. Torre, E. D. Fabrizio, O. F. Mohammed, A. Rothenberger, T. Wu, A. Gorirly, O. M. Bakr, *ACS Energy Lett.* **2017**, 2, 1782.

[34] H. Wang, C. Zhu, L. Liu, S. Ma, P. Liu, J. Wu, C. Shi, Q. Du, Y. Hao, S.

Xiang, H. Chen, P. Chen, Y. Bai, H. Zhou, Y. Li, Q. Chen, *Adv. Mater.* **2019**, 31, 1904408.

[35] M. Qin, K. Tse, T. K. Lau, Y. Li, C. J. Su, G. Yang, J. Chen, J. Zhu, U. S. Jeng, G. Li, H. Chen, X. Lu, *Adv. Mater.* **2019**, 31, 1901284.

[36] Y. Yang, L. Yang, S. Feng, Mater. Today Adv. **2020**, 6, 100068.

[37] J. Zhang, N. Kong, S. Uzun, A. Levitt, S. Seyedin, P. A. Lynch, S. Qin, M. Han, W. Yang, J. Liu, X. Wang, Y. Gogotsi, J. M. Razal, *Adv. Mater.* **2020**, 32, 2001093.

[38] K. Novoselov, o. A. Mishchenko, o. A. Carvalho, A. Castro Neto, *Science* **2016**, 353, aac9439.

[39] Y. Tang, Y. Zhang, H. Ouyang, M. Zhao, H. Hao, K. Wei, H. Li, Y. Sui, J. You, X. Zheng, Z. Xu, X. Cheng, L. Shi, T. Jiang, *Laser Photonics Rev.* **2020**, 14, 1900419.

[40] K. Wei, Y. Sui, Z. Xu, Y. Kang, J. You, Y. Tang, H. Li, Y. Ma, H. Ouyang, X. Zheng, X. Cheng, T. Jiang, *Nat. Commun.* **2020**, 11, 3876.

[41] L. L. Jiang, Z. K. Wang, M. Li, C. C. Zhang, Q. Q. Ye, K. H. Hu, D. Z. Lu, P. F. Fang, L. S. Liao, *Adv. Funct. Mater.* **2018**, 28, 1705875.

[42] S. A. Weber, I. M. Hermes, S.-H. Turren-Cruz, C. Gort, V. W. Bergmann, L. Gilson, A. Hagfeldt, M. Graetzel, W. Tress, R. Berger, *Energy Environ. Sci.* **2018**, 11, 2404.

[43] P. Cui, D. Wei, J. Ji, H. Huang, E. Jia, S. Dou, T. Wang, W. Wang, M. Li, *Nat. Energy* **2019**, 4, 150.

[44] Q. Dong, C. Zhu, M. Chen, C. Jiang, J. Guo, Y. Feng, Z. Dai, S. K. Yadavalli, M. Hu, X. Cao, Y. Li, Y. Huang, Z. Liu, Y. Shi, L. Wang, N. P. Padture, Y. Zhou, *Nat. Commun.* **2021**, 12, 973.

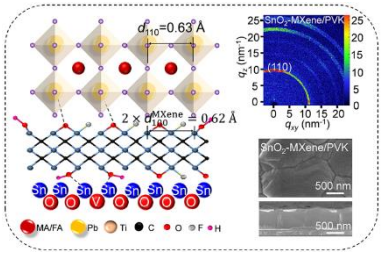
[45] V. Campanari, F. Martelli, A. Agresti, S. Pescetelli, N. Y. Nia, F. Di Giacomo, D. Catone, P. O'Keeffe, S. Turchini, B. Yang, J. Suo, A. Hagfeldt, A. D. Carlo, *Sol. RRL* **2022**, 6 2200049.

[46] D. Luo, W. Yang, Z. Wang, A. Sadhanala, Q. Hu, R. Su, R. Shivanna, G. F. Trindade, J. F. Watts, Z. Xu, T. Liu, K. Chen, F. Ye, P. Wu, L. Zhao, J. Wu, Y. Tu, Y. Zhang, X. Yang, W. Zhang,R. H. Friend, Q. Gong, H. J. Snaith, R. Zhu, *Science* **2018**, 360, 1442.

WILEY-VCH

RESEARCH ARTICLE

Entry for the Table of Contents



MXene nanosheets introduced to SnO_2-based perovskite solar cells maximize the interface matching between SnO_2 and perovskite and induce vertically aligned crystal growth. As a result, the photoelectric conversion efficiency (PCE) is improved by 15%, reaching 23.07%, and the short-circuit current is up to 25.07 mA cm^{-2}. In addition, an unencapsulated device maintains 90% of its initial PCE after 500 h of storage at 30–40% relative humidity in air.

WILEY-VCH